Open Ceramics 18 (2024) 100563

Contents lists available at ScienceDirect

Open Ceramics

journal homepage: www.sciencedirect.com/journal/open-ceramics

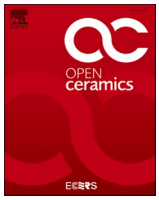

Composition dependence of oxidation resistance in high entropy ultra-high temperature ceramics

Lavina Backman [a,*], Joshua Gild [b,1], Mingde Qin [b], Jian Luo [b], Elizabeth J. Opila [a]

[a] Department of Materials Science & Engineering, University of Virginia, Charlottesville, VA, USA
[b] Department of NanoEngineering, University of California San Diego, La Jolla, CA, USA

ARTICLE INFO

Handling Editor: Dr P Colombo

Keywords:
High entropy
Ultra-high temperature ceramics
Carbides
Borides
Oxidation
Hypersonics

ABSTRACT

High entropy ultra-high temperature ceramics (HE-UHTCs) have garnered intense research interest due to the potential for optimized oxidation and mechanical properties for extreme environment applications. HE-UHTCs are expected to oxidize according to the thermodynamic favorability of their respective oxidation reactions, which varies according to the periodic grouping. Based on this, the oxidation resistance of equimolar (metals-basis) group IV + V (HfZrTiTaNb), group IV + V + VI (HfZrTiTaMo) and group IV + VI (HfZrTiMoW) carbides and borides were evaluated at 1700°C in 1 mol% O_2 for 5 min and compared. Group IV elements oxidized preferentially in all three compositions. Group V element-containing carbides exhibited the lowest oxidation resistance, attributed to the formation of intergranular liquid oxides. (HfZrTiMoW)C exhibited the best resistance among the carbides. The diborides exhibited similar material consumption, reinforcing the hypothesis that the oxidation behavior under these conditions is controlled by the presence of boria. These findings provide direction for HE-UHTC composition design for oxidation resistance.

1. Introduction

The oxidation mechanisms of group IV, V and VI carbides and diborides have been studied extensively due to their potential extreme environment applications [1], such as hypersonics and nuclear reactors. The high entropy design paradigm has been employed to broaden the compositional palette for UHTC carbides [2,3] and diborides [4]. The increased configurational entropy in high entropy materials has been credited with the stabilization of solid solution phases. In addition to the potential for improved mechanical and thermal properties, this expansion of compositional space could lead to the discovery of more oxidation resistant compositions.

The thermodynamic favorability of group IV oxides as well as their high melting temperatures suggest that designing an oxidation resistant high entropy ceramic from the collection of group IV, V and VI elements necessitates starting with Hf, Zr and Ti [5]. The other two ceramic components, assuming the choices are limited to the palette of group IV, V and VI transitional metals were chosen from Ta, Nb, Mo and W. Cr and V were not considered because their additions are expected to result in poor oxidation resistance at temperatures well below those under consideration. Cr–O vapor species have a high vapor pressure at the oxide/substrate interface, which compromises oxide scale adherence at temperatures as low as 980°C. Additionally, CrB_2 additions were found to be less effective than Ta or Nb-based additions in improving oxidation resistance [6]. Vanadium oxides have low melting temperatures[5] and form low-temperature melting eutectics with the oxides of the other elements under consideration, e.g. a eutectic in the ZrO_2–V_2O_5 is noted at 665°C [7], It is important to consider whether the thermodynamic considerations previously discussed [5,8] can be extended to compositions with group VI additions and determine whether they will oxidize to form volatile products. Therefore, a systematic study for the design of an oxidation resistant HE-UHTC, was considered as follows:

- **Composition 1:** Group IV + V elements, which form solid and liquid oxides, wherein liquid phase sintering could be promoted, but may be prone to the formation of oxides with low melting eutectics. The composition chosen for this was $(Hf_{0.2}Zr_{0.2}Ti_{0.2}Ta_{0.2}Nb_{0.2})X$ where X = C, B_2.
- **Composition 2:** Group IV + VI elements, which form solid and volatile oxides, i.e., the group VI elements will form volatile oxides which will leave the system, and the solid group IV oxides remain

* Corresponding author. Spacecraft Engineering Division, U.S. Naval Research Laboratory, 4555 Overlook Ave SW, Washington, DC, 20375, USA.
E-mail address: lavina.backman@nrl.navy.mil (L. Backman).
[1] Present address: Optical Sciences Division, U.S. Naval Research Laboratory, Washington, D.C.

https://doi.org/10.1016/j.oceram.2024.100563
Received 7 December 2023; Received in revised form 26 February 2024; Accepted 28 February 2024
Available online 7 March 2024

behind. The composition chosen for this was ($Hf_{0.2}Zr_{0.2}Ti_{0.2}Mo_{0.2}W_{0.2}$)X where X = C, B_2.

- **Composition 3:** Group IV + V + VI elements. The composition chosen for this was ($Hf_{0.2}Zr_{0.2}Ti_{0.2}Ta_{0.2}Mo_{0.2}$)X where X = C, B_2.

As all compositions chosen were equimolar, the subscript "0.2" in the composition identification will be dropped for ease of reading; thus (HfZrTiTaNb)C is equivalent to ($Hf_{0.2}Zr_{0.2}Ti_{0.2}Ta_{0.2}Nb_{0.2}$)C.

In prior work [8,9] that presented the results for Composition 1, the preferential oxidation of one or more components was predicted and verified. The high entropy compositions (HfZrTiTaNb)C and (HfZrTiTaNb)B_2 tested did not oxidize uniformly. At 1700°C, the high entropy approach appeared to be detrimental to the oxidation resistance of the material, as demonstrated by the extensive grain boundary oxidation. If a high entropy material is stabilized by configurational entropy, it stands to reason that preferential oxidation occurring in an oxidizing environment will deplete the substrate of one or more constituents and destabilize the solid solution. It is not clear how the changing substrate composition affects the oxidation mechanisms and kinetics of HE-UHTC carbide and borides.

The objectives of this study were to (a) determine the oxidation resistance of HfZrTiTaMo and HfZrTiMoW carbides and borides by measuring material consumption after tests in similar conditions, and then comparing these to the group IV + V compounds (Hf, Zr, Ti, Ta and Nb), the results of which were previously published [9]; (b) explore the compositional effects on the oxidation resistance as described by the periodic trends previously observed; (c) determine whether the preferential oxidation behavior is also observed in other compositions.

1.1. Expected oxidation behavior of group IV compounds with group V and VI additions

HfC, ZrC and TiC form mainly HfO_2, ZrO_2 and TiO_2 respectively. Additionally, solid solution refractory metal ceramics such as (Hf,Ta)C [10,11], and other solid solution or composite carbide- and boride materials [12,13] form complex oxides such as $Hf_6Ta_2O_{17}$. An oxycarbide interlayer has been reported for the three group IV oxides, although the exact nature of this interlayer has been debated [14]. In the case of TiC, Ti suboxides are also predicted (See Supplement) to be stable, and have been observed to form as additional products [15,16]. Oxidation studies of TaC [17] as well as HfC-TaC solutions [10] report the formation of an oxycarbide. Szökefalvi-Nagy and Jehn [18] observed the formation of a metal layer at the oxide-gas interface on TaC at higher temperatures (1827°-2000°C). At temperatures at or above 1500°C, the oxidation of TaB_2 resulted in the formation of Ta oxides, which were reported to have volatilized [19]. Kofstad also observed weight loss due to volatilization during the high temperature oxidation of tantalum [20]. Silvestroni et al. [19] proposed, based on the work of Jehn and Olzi [21], that the dissociation of Ta_2O_5 into α-Ta and a volatile liquid phase occurs above 1600°C.

Group V additions to group IV ceramics in various forms, mainly as Ta compounds, have resulted in some limited improvement in oxidation behavior, whether through liquid phase assisted sintering of the group IV oxides, the doping of group IV oxides with higher valence ions to limit oxygen transport through oxygen vacancies [13], or the formation of ordered compounds such as $A_6B_2O_{17}$ (A = Hf, Zr; B = Ta, Nb) [13,22] (Fig. 1(a)). On the other hand, liquid oxide formation at more aggressive conditions and ultra-high temperatures has been shown to be detrimental to the oxidation behavior of UHTCs. Results discussed in previous work [9] for the group IV + V combination shows that the oxidation behavior of the solid solution closely matches the design considerations [5] from the constituent elements, i.e., the formation of group V oxides, for example, promoted the formation of oxides with low melting temperatures that resulted in a decrease in oxidation resistance of the material.

The addition of the group VI element molybdenum to Hf and Zr

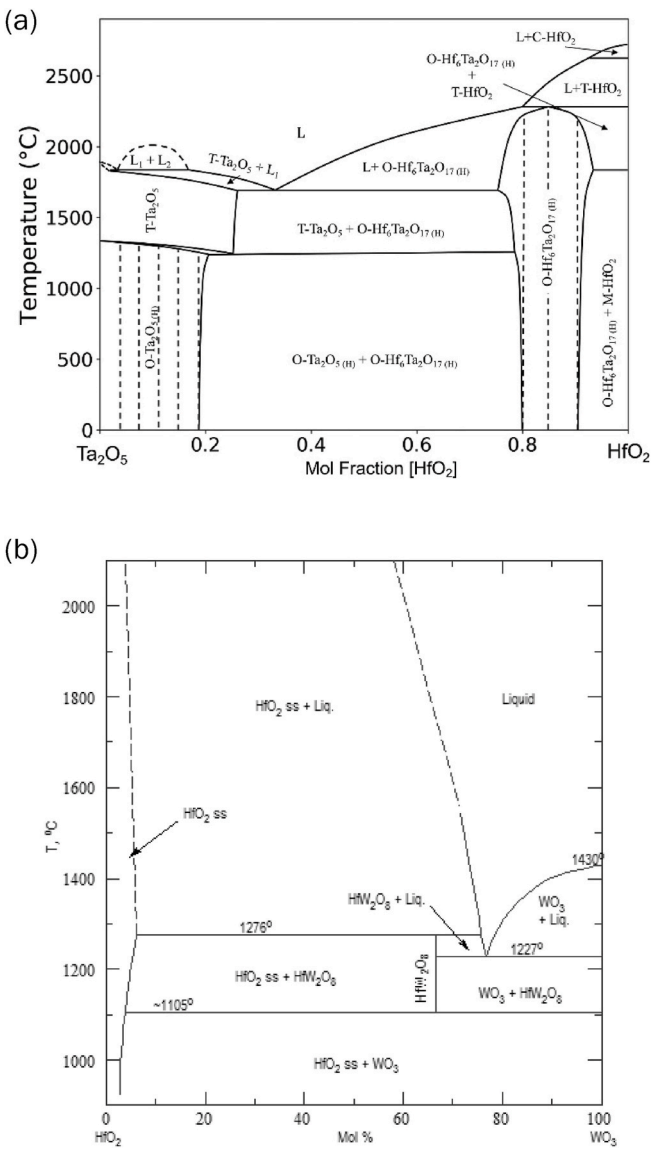

Fig. 1. Pseudobinary phase diagram for (a) HfO_2-Ta_2O_5 from McCormack et al. [47], and (b) HfO_2-WO_3 from Chang et al. [37] and obtained from the Phase Equilibria Diagrams Database (NIST Standard Reference Database 31), The American Ceramic Society and the National Institute of Standards and Technology, 2020. Figure Number 04445.

based UHTCs has mainly been in the form of $MoSi_2$ [23–28]. The oxidation behavior of $MoSi_2$ containing boride materials has typically been characterized by the observation of silica along with the group IV rich condensed phase oxide [29], although small amounts of condensed MoO_x and MoO_3 have been observed [30]. Materials containing boron typically form a borosilicate glass along with Mo–B rich phase [26,27,30], which have been credited with the increased oxidation resistance. However at ultra-high temperatures (1800°C), the borosilicate glass layer is "turbulent" due to the evolution of the gaseous Si, B and Mo oxides [30], suggesting that the formation of a scale may be disrupted by these volatile gases. Dehdashti et al. [31] explored the addition of Mo to ZrB_2 and found that Mo in the boria scale stabilized the boria scale at higher temperatures, resulting in improved oxidation resistance. The Hf and Zr carbides with $MoSi_2$ additions have been characterized by porous scales and it is thought that volatile Mo oxides escape through these pores [29]. A ZrC–Mo cermet was tested and found to form MoO_3, which readily volatilizes; additionally, spallation of the oxide scale [32] was observed.

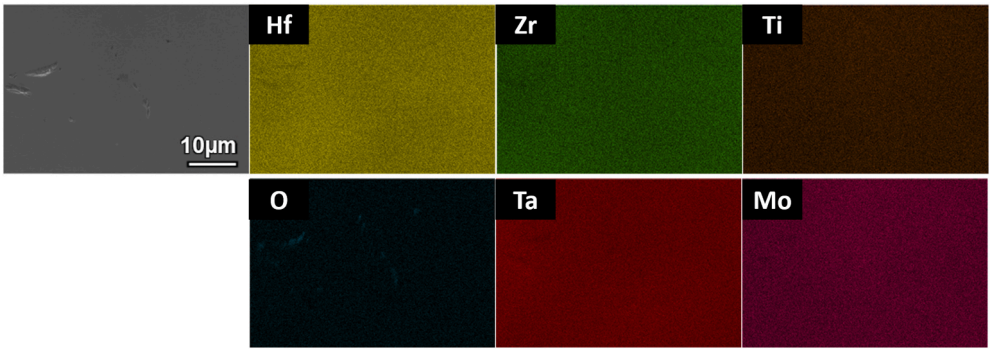

Fig. 2. Secondary electron image and EDS maps for (HfZrTiTaMo)C before oxidation.

W additions to ZrB_2 have been explored, and it was found that W additions improved the oxidation resistance of ZrB_2 [33]; this improved resistance was, similar to studies with Mo, attributed to higher stability of the liquid boria. WC and WB additions to HfB_2-SiC were found to improve oxidation resistance of HfB_2-SiC at 2000°C by promoting liquid phase sintering of the HfO_2 scale [34]. Similarly, the improved oxidation resistance of ZrB_2 with WC additions was attributed to the W-assisted densification of the ZrO_2 rich scale [35], although this was later questioned after detailed microstructural analysis performed by Silvestroni et al. [36].

Phase diagrams for the oxides of Mo and Hf, or Mo and Zr, are not available. However, the phase diagrams for W oxides and HfO_2 (shown for reference in Fig. 1(b)), as well as W oxides and ZrO_2 exist and show limited solubility of the W oxide in the group IV oxides [37]. Complex oxide formation is possible, as are low melting eutectics (>1231°C). The coexistence of HfO_2 and W oxides as separate phases at temperatures higher than this, along with the volatility of W oxides, suggest that W oxides would readily volatilize, leaving behind HfO_2 (and by similitude, likely ZrO_2).

Equations (1) and (2) describe the expected generalized form of the reactions that take place upon exposure of carbides and borides, respectively, to oxidizing environments at high temperatures.

$$\frac{2}{b+1}MC + O_2(g) \leftrightarrow \frac{2}{b+1}MO_b + \frac{2}{b+1}CO(g) \quad (1)$$

$$\frac{2}{b+3}MB_2 + O_2(g) \leftrightarrow \frac{2}{b+3}MO_b + \frac{2}{b+3}B_2O_3(l,g) \quad (2)$$

During the oxidation of carbides at high temperatures, gaseous products such as CO(g) are released, which results in a porous, non-protective oxide scale [38]. The oxidation of borides results in the formation of liquid boria which has been reported to boil at T = 1860°C [39,40]. The rate limiting mechanism for group IV metal diborides is expected to be oxygen transport through boria-filled pores and channels in the refractory oxide [41]. However, it is hypothesized that the protectiveness due to liquid boria is limited to temperatures below about 1850°C; above this temperature, Parthasarathy et al.'s model has shown boria to volatilize as soon as it forms [39,41]. This skeleton/pore-filling microstructure is not seen for the group V diborides [19]. It is unclear at this time whether the better candidate for an oxidation resistant HE-UHTC operating at ultra-high temperatures is a carbide or boride.

2. Methodology

The (HfZrTiTaMo)C and (HfZrTiMoW)C compositions were synthesized by sintering commercial powders in the same manner as previously described [9]. The (HfZrTiTaMo)B_2 composition was synthesized by sintering powders made via borocarbothermal reduction, also previously described [9]. The (HfZrTiMoW)B_2 was synthesized by adding 1 wt% graphite to TiB_2, ZrB_2, MoB_2, HfB_2 and W_2B_5 commercial powders, and performing a high energy ball milling step prior to consolidation via SPS. The elemental distribution and XRD patterns for the high entropy compounds prior to oxidation are of interest and presented in the results. These spark-plasma sintered pellets were then machined into the dog-bone configuration (Bomas Machine Specialties, Somerville, MA), and tested using the resistive heating system [9]. As with the group IV + V compounds [9], the IV + V + VI and IV + VI carbides and diborides were ramped to temperature in flowing (~1 L/min) ultra-high purity argon (2 vol-ppm O_2 impurity max, Praxair, Danbury, CT). Once the test temperature was achieved certified 1 vol% O_2 (balance argon) gas (Praxair, Danbury, CT) was turned on (~1 L/min). Isothermal oxidation exposures were conducted for 5 minutes from the time the oxidizing gas began to flow [9]. The low partial pressures of oxygen used result in lower oxidation rates allowing for longer exposures and time dependent studies (described in future publication: Backman, L., Graham, K., Dion, M. Opila, E.J., manuscript submitted for review). Additionally, it is expected that the application conditions for these materials are likely to be at higher altitudes, which correspond to lower pO_2. After oxidation exposures, all samples were fractured in the pyrometer sighting zone, where the temperature of the sample is known. The cross-sections were examined using scanning electron microscopy (SEM, FEI Quanta 650, FEI-Thermo Fisher Scientific, Hillsboro, Oregon) and energy dispersive spectroscopy (EDS, Oxford Instruments Aztec X-Max^N 150, Concord, MA). The material consumption was measured by taking at least ten measurements of the thickness of the remaining unoxidized cross-section, then subtracting this value from the thickness of the material before oxidation exposures. The determination of the unoxidized region was made by comparing oxygen EDS maps with secondary and backscattered electron images. Fracture cross-sections were utilized i) to avoid difficulty in distinguishing carbide areas from epoxy impregnated oxides by EDS-carbon analysis, and ii) to avoid preferential loss of soft oxide relative to hard carbides during sample polishing. The oxidized samples were also characterized using X-ray diffraction (XRD, PANalytical Empyrean, Almelo, The Netherlands), using conventional powder diffraction and micro-focusing optics, in the 20-to-80-degree 2θ range. With the micro-focusing optics, the beam size was constrained to be 720 μm in diameter and focused on the pyrometer sighting zone, which has an approximate size of 1.5 mm in diameter [9].

3. Results

3.1. As-received materials

3.1.1. High entropy carbides

Fig. 2 shows generally even distribution of all the metallic species in (HfZrTiTaMo)C. Some intensity variation is noted for hafnium and molybdenum. Analysis of the XRD pattern (Fig. 3) shows only one set of peaks consistent with rocksalt structure, although some asymmetry is observed, especially at higher two-theta angles. Analysis during peak fitting indicates that this asymmetry may be due to lattice parameter

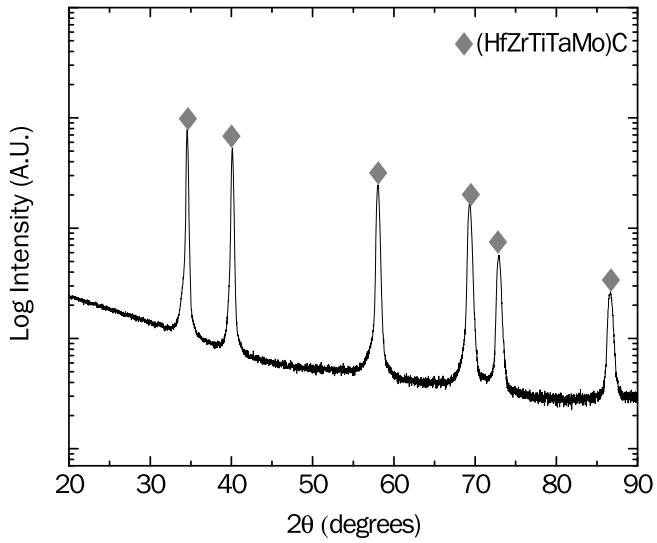

Fig. 3. XRD pattern obtained from (HfZrTiTaMo)C before oxidation showing one set of peaks.

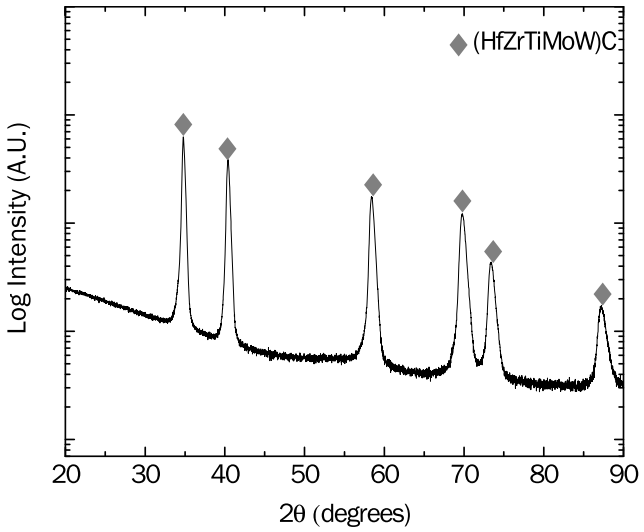

Fig. 5. XRD pattern obtained from (HfZrTiMoW)C before oxidation showing one set of peaks.

variation associated with compositional inhomogeneity in the specimen (Fig. 2). No peaks due to retained Hf and Zr oxides are observed.

Fig. 4 shows slight chemical inhomogeneity of the metallic species in the (HfZrTiMoW)C sample. One phase appears to be rich in Hf and Zr, another rich in Mo and Ti, and possibly third rich in Ti and W. Analysis of the XRD pattern (Fig. 5) shows only one set of peaks consistent with the rocksalt structures, although these peaks appear broad and asymmetric, especially at higher two-theta angles. Similar to the (HfZrTiTaMo)C case, the asymmetry observed may be due to slight lattice parameter variation. No peaks due to retained Hf and Zr oxides are observed.

3.1.2. *High entropy borides*

The high entropy diboride (HfZrTiTaMo)B_2 exhibited uniform elemental distribution of all the metallic elements (Fig. 6) and relative densities of 99% or greater, with less than 1 vol% of B_4C retained as a secondary phase, as described by Gild et al. [42]. A single-phase high entropy diboride is confirmed by XRD analysis (Fig. 7) showing the hexagonal AlB_2-type structure.

The (HfZrTiMoW)B_2 composition does not form a single-phase diboride. At least one W-rich second phase was observed. The elemental distribution of the phases is shown in Fig. 8. The XRD pattern also confirms the presence of a second boride phase, apparent as the bright phase in Fig. 8, the approximate composition of which is given by point EDS analysis (Fig. 9). These results show that the main diboride phase is deficient in Mo and W, relative to the equimolar case, and is richer in the group IV elements. The second phase is rich in W, contains roughly equal amounts of Mo and Ti, and to a slightly lesser extent Hf and Zr. Based on analysis completed via image processing, it was determined that the W-rich phase constitutes 10.5 ± 1.6 vol%. The material also had residual graphite, which was evaluated to be 1.2 ± 0.3 vol%. The elemental distributions in Fig. 8 also indicate possible clustering of Mo and Zr in the main diboride phase.

3.2. *Oxidation results*

A quantitative comparison of material consumption for all high entropy compositions is provided (Table 1, Fig. 10) for 5-min exposures at 1700°C in 1%O_2. The results show that the borides consistently exhibited better oxidation resistance under these conditions compared to the carbides. The different boride compositions also performed similarly, when compared with each other. The material consumption values for the high entropy carbide compositions generally exhibited poorer oxidation resistance. (HfZrTiMoW)C exhibited the lowest material consumption among all high entropy carbides. (HfZrTiTaMo)C, the group IV + V + VI composition, exhibited the highest material consumption. The oxidation products and microstructure will be discussed in more detail in the following sections.

3.2.1. *High entropy carbide oxidation*

The group IV + VI composition, (HfZrTiMoW)C, exhibited better oxidation resistance compared to the group IV + V composition, (HfZrTiTaNb)C. The oxide formed on (HfZrTiMoW)C is mostly dense, although a few cracks and pores were observed (See Supplement

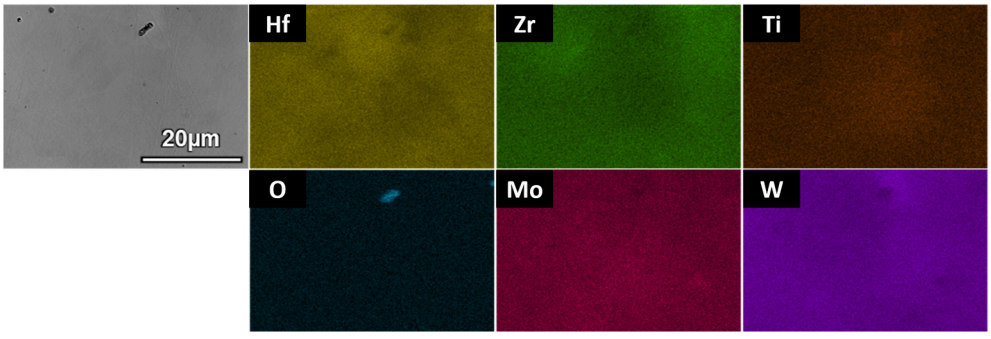

Fig. 4. Secondary electron image and EDS maps for (HfZrTiMoW)C before oxidation, showing slight inhomogeneity.

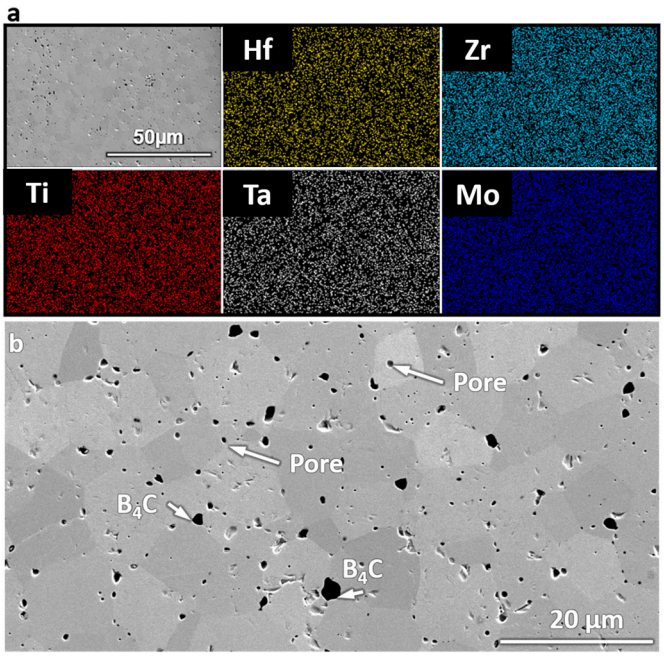

Fig. 6. (a) Secondary electron image and EDS maps for $(HfZrTiTaMo)B_2$ before oxidation. (b) Higher magnification secondary electron image taken for $(HfZrTiTaMo)B_2$ before oxidation.

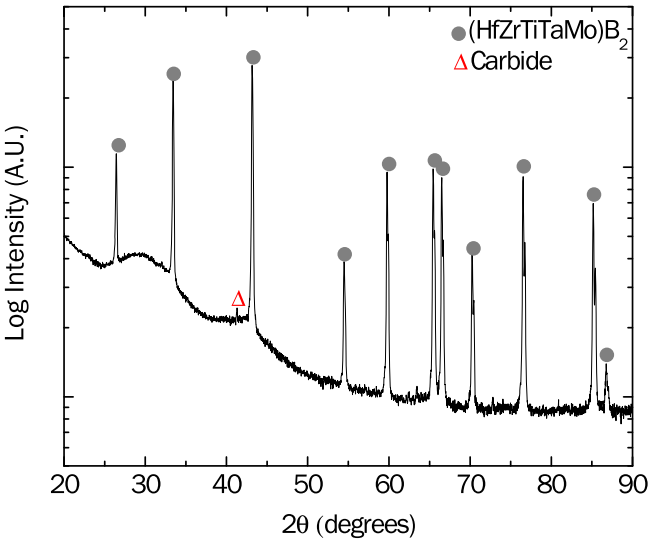

Fig. 7. XRD pattern for $(HfZrTiTaMo)B_2$ before oxidation showing one set of peaks.

Figure S2). A higher magnification plan view image shows that the oxide scale consists of two phases: one that is oxygen rich and contains group IV elements, and one that is oxygen-lean and contains Mo and W (Fig. 11).

The fracture cross-section view of the oxidized (HfZrTiMoW)C is shown in Fig. 12 at the oxide-gas interface. An oxidized region on the surface appears dark in the back-scattered electron image (Fig. 12 (a)). At higher magnification, the back-scattered electron image shown in Fig. 12 (b) shows discrete VI-rich grains surrounded by continuous group IV-rich oxides, as we had seen in the plan view images as well (Fig. 11). The surface microstructure is present at varying depths in the oxidized region starting at the oxide/gas interface. This region is best highlighted by the Hf and Mo maps, as well as the layered map shown. Below or near this two-phase region, the grains have uniform morphology and contrast (in backscatter). EDS mapping shows that all elements are present in the single-phase oxidized or partially oxidized region. Fig. 12 (a) shows how far O has penetrated into the substrate, and Fig. 12 (b) shows the two-phase region at the top of the scale. Due to topography, it is difficult to determine the extent of O intensity variation within the oxidized region shown. The two-phase region also exhibits some porosity through its thickness.

The two-phase Mo-rich/Hf-rich region seen on the surface and shown in Fig. 12(b) also appears at what may be former grain boundaries. Fig. 13 shows this, as well as elemental analysis showing that the phases are a group IV-rich oxide and a group VI-rich partially oxidized carbide. Based on examination of the oxide-substrate interface, oxygen is transported from the surface, to grain boundaries and into the grain (See Supplement Figure S4).

A two-phase oxidized region is also observed, with the group IV elements selectively oxidizing to form Hf, Zr and Ti oxides, leaving behind Mo-rich carbides or oxycarbides as confirmed by XRD (See Supplement Figure S5). XRD analysis for these materials is challenging at best due to multiple possible peak overlaps. Additionally, it is difficult to distinguish between rocksalt carbide or oxycarbide. The XRD results should therefore be considered with caution, although the results appear consistent with EDS results.

The group IV + V + VI carbide, (HfZrTiTaMo)C, which exhibited the highest material consumption of the compositions tested, also shows a two-phase microstructure on the surface (Fig. 14). The brighter phase is oxygen deficient and likely a carbide containing mostly Mo and some Ta. The oxide phase is mostly rich in Hf, Zr and Ti, with minimal amounts (~1 at%) of Ta (Fig. 14).

The cross-section view (Fig. 15) shows a two-phase oxidized region as well. The oxide-rich regions near the surface appear to have somewhat less porosity than (HfZrTiMoW)C (Fig. 12(b)–. 13), particularly around the bright grains seen in Fig. 15 (a), where they appear quite dense. Intergranular voids, however, were observed. Near these intergranular voids, rounded features consistent with possible solidified melt were observed (Fig. 15 (a)). One of the phases has an elemental composition (Fig. 15 (c)) similar to the dark gray oxide region on the surface shown in Fig. 14, containing Hf, Zr and Ti, with ~1–2 at% Ta. The second phase is Mo and Ta rich, and O deficient (Fig. 15 (d)). XRD analysis (See Supplement Figure S6) is consistent with a (Mo,Ta)C phase

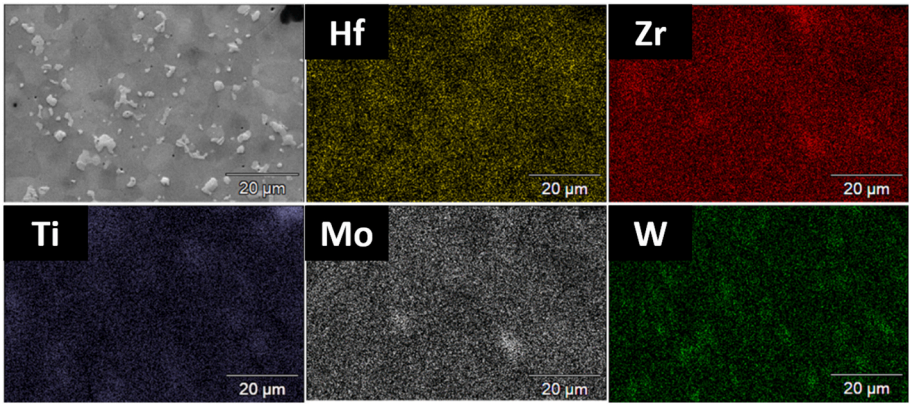

Fig. 8. Secondary electron image and EDS maps for $(HfZrTiMoW)B_2$ before oxidation.

present along with Hf, Zr and Ti rich oxides. Fig. 16 shows a similar region in the (HfZrTiTaNb)C oxidized under the same conditions, for comparison. This composition exhibits similar morphology indicating solidified melts and intergranular voids.

Both (HfZrTiMoW)C and (HfZrTiTaMo)C exhibit intergranular oxidation. Fig. 17 shows the oxide/substrate interface in cross-section exhibiting oxidation along the grain boundaries, which was also observed for (HfZrTiTaNb)C [9] (Fig. 16).

3.2.2. *High entropy diboride oxidation*

The oxidized surface of $(HfZrTiTaMo)B_2$ exhibited bubbles and dark contrast, glassy appearing regions that are likely solidified boria melt (See Supplement Figure S7). Examination of the oxide scale in the pyrometer sighting zone at higher magnification (Fig. 18) shows the oxide is mostly composed of group IV elements, most notably Hf and Zr. Bubbles and cracks were also observed. Minimal Mo and Ta-containing phases are observed on the surface, in contrast with the carbide case. The Mo-rich phase also appears to contain B (Fig. 18 (b)) and is deficient in O, indicating a Mo boride phase on the surface. XRD data (See Supplement Figure S8) also indicates that MoB exists in oxidized region; however, XRD could be detecting phases beneath the surface. XRD analysis also indicates that the oxide consists primarily of group IV elements, although a small Ta_2O_5 peak appears. The primary oxide phase is HfO_2, which could be $(Hf,Zr,Ti)O_2$ based on EDS data. EDS analysis of the specimen in fracture cross-section (Fig. 19) also shows Mo and Ta rich grains that could be (Mo,Ta)B or $(Mo,Ta)B_2$.

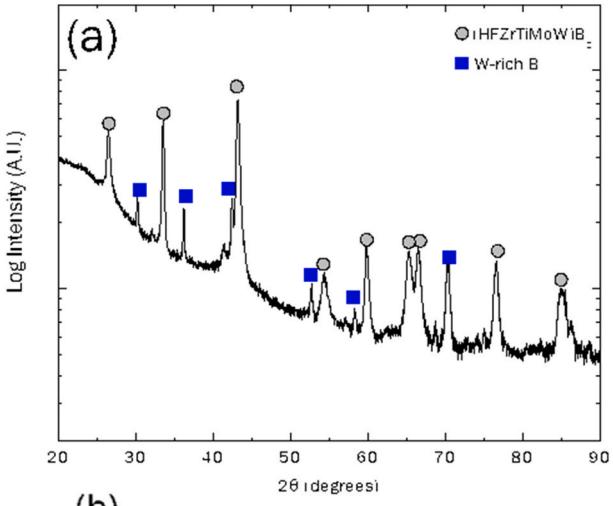

(b)

Cation	Diboride Phase At.%	W-rich boride At.%
Ti	22.4%	17.1%
Zr	25.4%	14.1%
Mo	14.7%	18.4%
Hf	22.2%	13.2%
W	15.3%	37.2%

Fig. 9. (a) XRD pattern for $(HfZrTiMoW)B_2$ before oxidation, (b) Point EDS analysis showing approximate breakdown of elemental concentration in each phase.

Table 1
Material consumption values measured for different compositions tested at 1700°C in 1% O_2 for 5 min.

Material	Material Consumption (μm)	Std. Dev. (μm)
Carbides		
(HfZrTiTaNb)C	125	5
(HfZrTiTaMo)C	155	13
(HfZrTiMoW)C	95	9
Borides		
(HfZrTiTaNb)B_2	50	4
(HfZrTiTaMo)B_2	62	4
(HfZrTiMoW)B_2	55	2

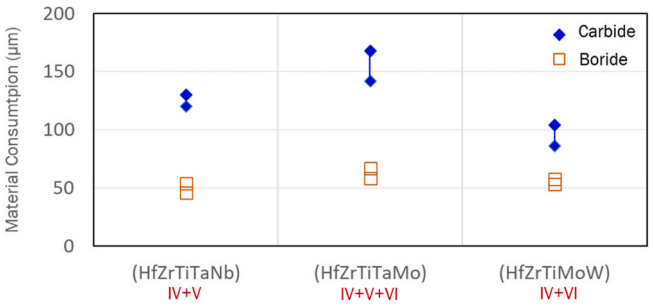

Fig. 10. Plot showing material consumption measured for compositions tested at 1700°C in 1% O_2 for 5 min. Each data "point" is a range of values covering the average and standard deviation of measured material consumption. Closed blue diamonds indicate carbides and open orange squares indicate diborides.

The surface layer contains mostly Hf and Zr oxide, beneath which a void can be seen that may contain boria. Beneath this void, a fine-grained, partially oxidized region exists, depleted in Hf and Zr. The bright, fine grains shown in the partially oxidized region in Fig. 19 are primarily rich in Mo and Ta, contain very little (~1–3 at% Ti) and are deficient in O.

Like the (HfZrTiTaMo)B_2 samples, the surface of the (HfZrTiMoW)B_2 sample shows possible retained boria and bubble formation, indicating escape of gaseous oxides (See Supplement Figure S9). SEM and EDS point analysis show that the surface oxide in the pyrometer sighting zone consists of Hf, Zr and Ti oxide (Fig. 20). The secondary W-rich phase, present in the pre-oxidized specimen appears to be retained even at the surface. As boron is both difficult to detect via EDS and has some overlap with zirconium's low-energy M peak, EDS analysis is not conclusive as to the extent of oxidation of this secondary phase.

Examination of the specimen fracture cross-section (Fig. 21) after oxidation shows the W-rich secondary phase to be present in the oxidized region, and the matrix (high entropy diboride phase) to have oxidized around it. An external scale consisting of group IV elements, like the (HfZrTiTaMo)B_2 sample, is apparent, as is the fine scale microstructure in the oxidation affected zone. Voids are also present underneath the external oxide scale. XRD analysis (See Supplement Figure S10) confirms that a HfO_2 scale formed (likely (Hf,Zr,Ti)O_2), and coexists with W-rich borides, including the secondary phase from the pre-oxidized sample.

4. Discussion

4.1. Carbides

(HfZrTiTaNb)C, (HfZrTiTaMo)C and (HfZrTiMoW)C oxidize preferentially according to the relative thermodynamic favorabilities [8], with group IV oxides dominating in the oxide scales, and Ta, Mo and W (in their respective materials) following. This is not to say that at these conditions, the group V and VI elements did not oxidize. Evidence for Ta_2O_5 is seen in XRD data as well as evidence of Mo and W oxides (See Supplement). (HfZrTiMoW)C exhibited lower material consumption compared to the other high entropy compositions. While the surface on (HfZrTiMoW)C exhibits a mostly dense scale (Fig. 11), examination in cross-section reveals some porosity just below the surface and the presence of fine particles of group VI (Mo,W) carbide phase. Oxidation of this phase results in volatile oxides that leave the system [5], which was expected. Both Mo and W were observed in the deposits in the cooler regions of the experimental set-up, e.g., chamber walls and clips holding the sample, suggesting that both group VI elements had at least begun oxidizing (we still see remnants of Mo and W containing carbide on the surface). More Mo is observed in these downstream deposits, which may be an indication of Mo oxides being more volatile than W oxides as proposed through thermochemical analyses [43]. W additions are also known to promote densification of the group IV oxides [34,36], and these may explain the mostly dense appearance of the group IV-rich oxide, particularly around the group VI-rich carbide grains. Overall, this behavior led to a more uniform attack and may be partially responsible for the lower material consumption observed for (HfZrTiMoW)C.

Although all samples exhibited intergranular oxidation, the group V

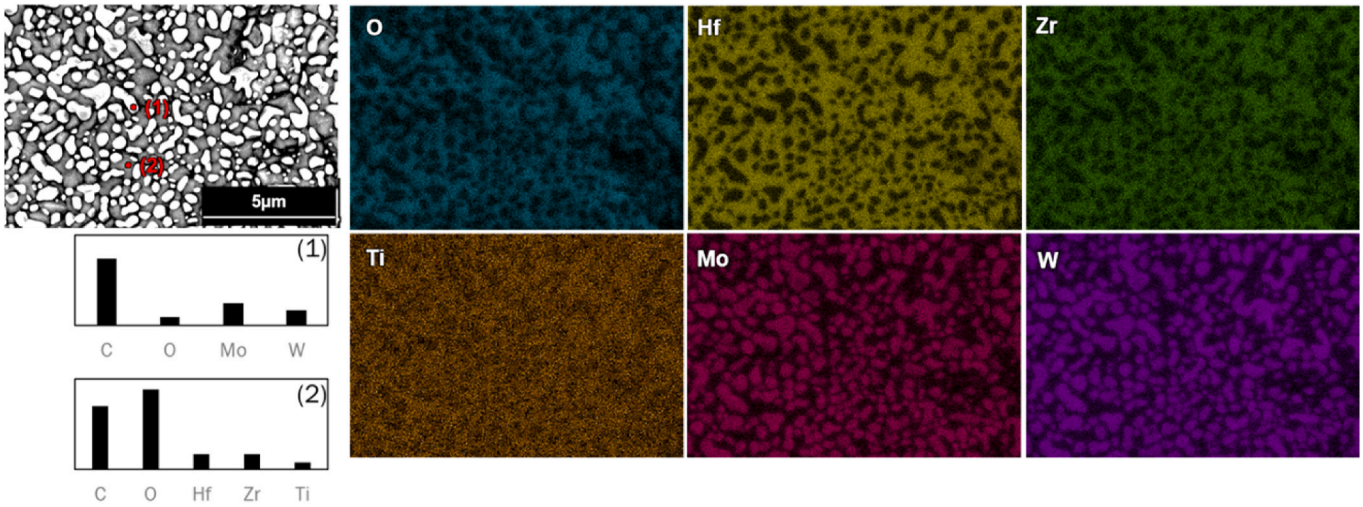

Fig. 11. (Top Left) Back-scattered electron image in plan view of the oxide formed in the pyrometer sighting zone on (HfZrTiMoW)C after exposure to 1%O_2 at 1700°C for 5 min, along with (Bottom Left) EDS point analysis (arbitrary units) showing the relative elemental composition of the two phases present, (a) and (b). {Right) EDS elemental maps of the same region.

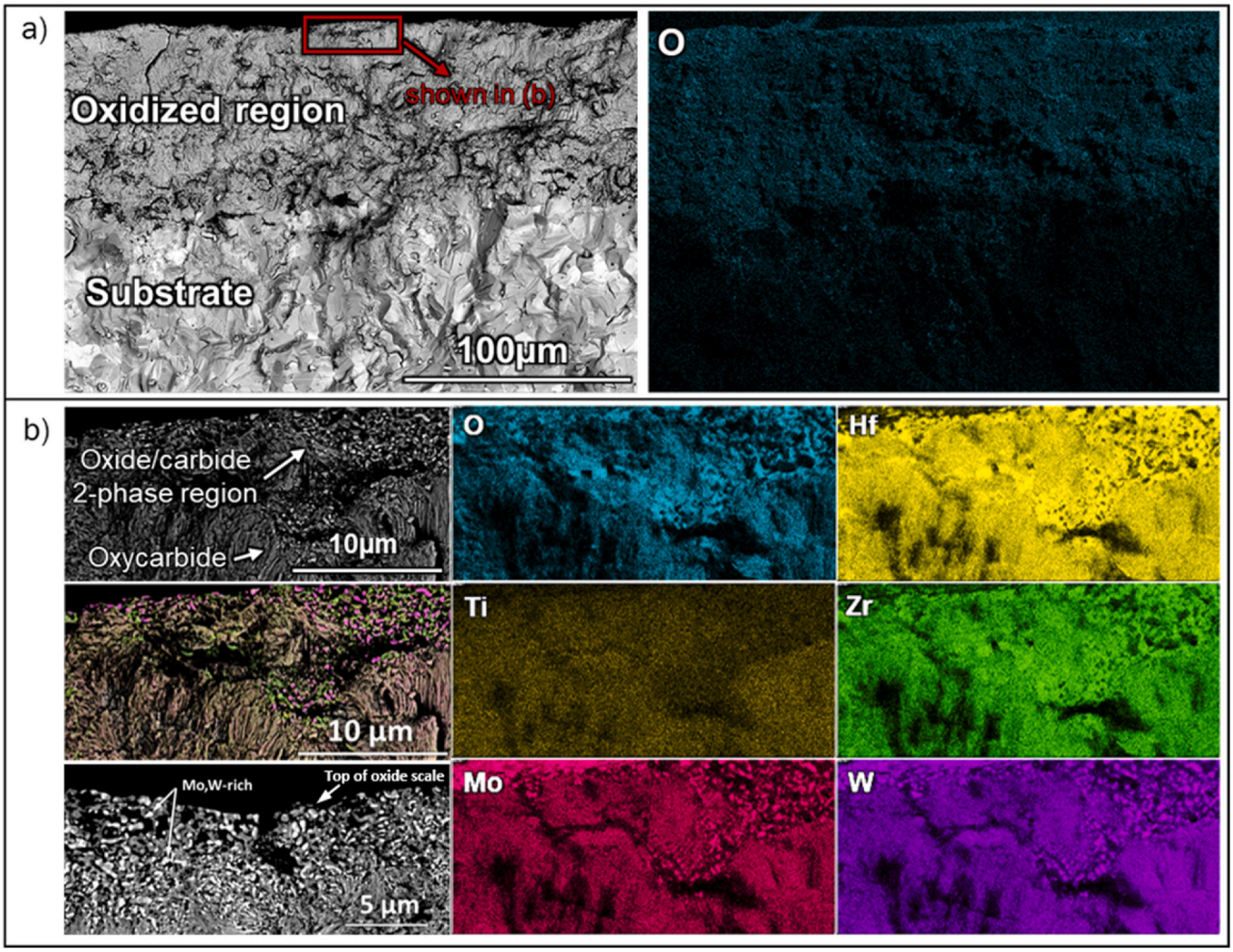

Fig. 12. Electron image and elemental maps fracture cross-section view, of (HfZrTiMoW)C oxidized at 1700°C in 1%O_2/Ar for 5 min. (a) Lower magnification back-scattered electron image and oxygen map, (b) Higher magnification images of the top of the oxide scale (near gas/oxide interface) along with Hf, Zr, Ti, Mo, W, and overlaid elemental maps.

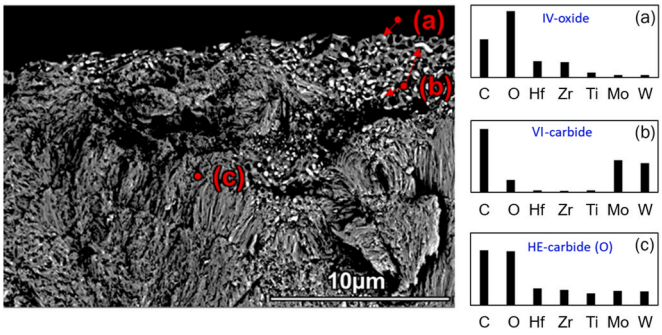

Fig. 13. High magnification back-scattered electron image, fracture cross-section view, of (HfZrTiMoW)C oxidized at 1700°C in 1%O_2/Ar for 5 min, and EDS point analysis for (a) the dark phase at the top of the scale, (b) the bright phase at the top of the scale, and (c) the partially oxidized single phase high entropy carbide region adjacent to the two-phase region.

containing compositions exhibited higher material consumption than (HfZrTiMoW)C. Both (HfZrTiTaNb)C and (HfZrTiTaMo)C exhibited voids at grain boundaries and evidence of liquid oxide formation (Figs. 15 and 16). Low melting oxide phases and eutectics exist in the oxide systems containing group IV and V elements. Nb oxides and eutectics of Nb oxides melt below 1500°C (Nb_2O_5–TiO_2 eutectics from 1467° to 1477°C [44], Nb_2O_5–ZrO_2 eutectics at 1436°C [45]). Ta oxides in addition to Nb oxides result in liquid oxide formation below 1700°C, (Ta_2O_5–TiO_2 eutectic at 1621°C, Tm for $TiTa_2O_7$ is 1674°C [46]). These low-melting complex oxides due to the group V elemental additions (e.g. $TiTa_2O_7$) persist, assist in the densification of group IV-oxides that form along grain boundaries. Once these are densified, the formation of any

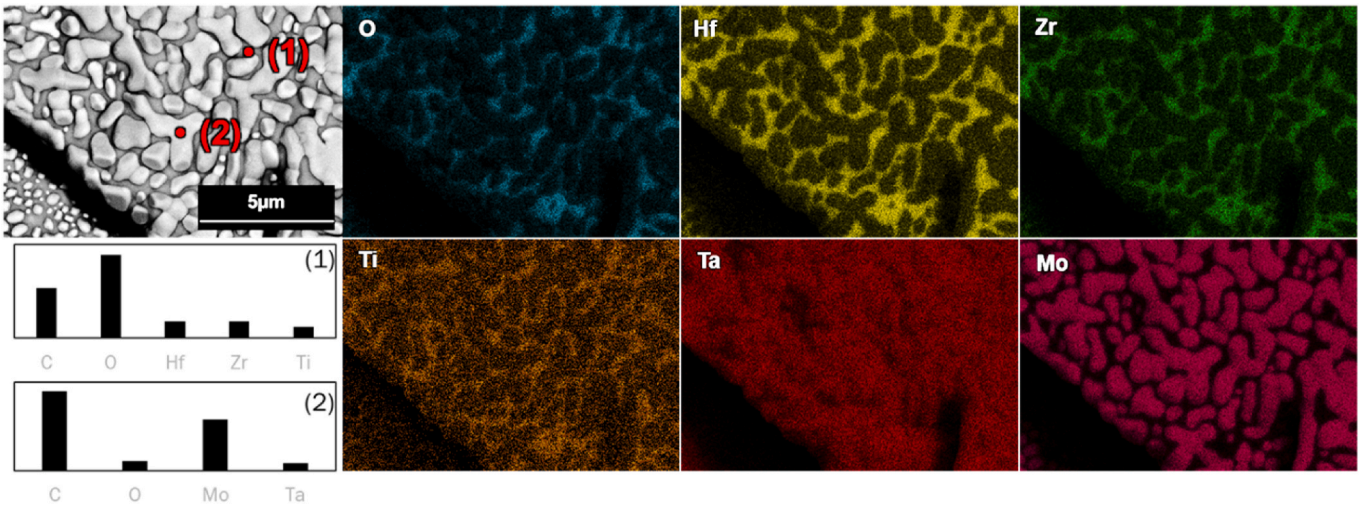

Fig. 14. (Top Left) Back-scattered electron image in plan view of (HfZrTiTaMo)C oxidized at 1700°C in 1%O_2 for 5 min, (Bottom Left) EDS point analysis (arbitrary units) of the relative elemental compositions of the (1) dark, oxide phase and (2) bright, carbide phase. (Right) Elemental EDS maps.

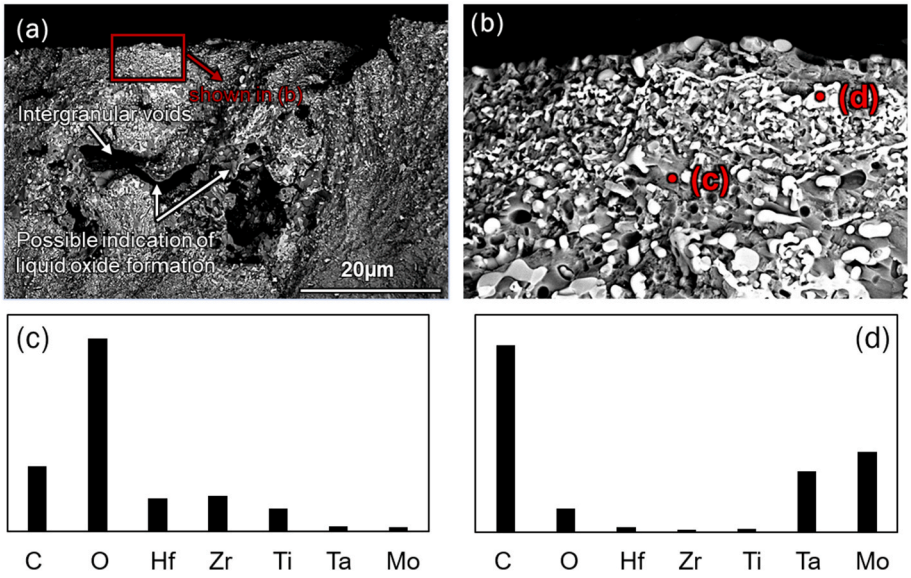

Fig. 15. Fracture cross-sections of (HfZrTiTaMo)C oxidized at 1700°C in 1%O_2/Ar for 5 min. (a) lower magnification back-scattered electron image of the oxidized region at the oxide/gas interface; (b) higher magnification back-scattered electron image of the oxidized region at the oxide/gas interface; (c) and (d) show point EDS analysis (arbitrary units) of the relative elemental composition of the dark and bright regions in (b), respectively. Each EDS data set is averaged over a minimum of five like points.

gaseous oxides (e.g. CO(g)) results in large voids that accelerate the oxidation ingress, and therefore material consumption. In contrast, W (and potentially Mo) oxides show limited solubility in group IV oxides (example phase diagram shown in Fig. 1), and although are liquid at the test temperature they readily volatilize, especially at 1700°C. The result is *transient* densification due to liquid phase assisted sintering of the group IV oxides that have formed, then volatilization of the group VI oxides without persistent liquid oxide formation. Ta_2O_5 is not as volatile (see Supplement) and forms solid solutions or ordered compounds with group IV oxides [47], which means that at the high temperatures of interest, it can persist in the oxide scale and promote liquid oxide formation. Any volatility that Ta-based species may exhibit would further the deleterious effect of forming voids in the intergranular regions. In (HfZrTiTaMo)C, the combined formation of liquid oxides that helped densify oxides around grain boundaries with volatile oxides (Mo oxides, CO(g)) resulted in large intergranular voids that led to higher material consumption due to oxidation.

The morphology and composition of the oxides formed on (HfZrTiMoW)C, e.g. Fig. 13 (point c), suggest that the material oxidizes by way of oxygen dissolution and transport in the high entropy carbide grain. Similar morphology is seen in (HfZrTiTaMo)C (Fig. 15(a)). The preferential oxidation of group IV elements then leaves behind group IV-element and C-rich grains. We see this near the oxide-gas interfaces (grain boundaries and the top of the scale, see two-phase regions in Fig. 13). Apparent oxygen dissolution in the high entropy carbide phase was not observed for (HfZrTiTaNb)C [9] to the extent and depth that was apparent for (HfZrTiTaMo)C and (HfZrTiMoW)C. The extent of oxygen dissolution in the group VI carbides is not well known. Observations of oxygen dissolution in group VI carbides are not reported in the literature [48–51], and an understanding of the dissolution of oxygen in refractory carbides and the formation of oxycarbides is a key knowledge gap in the area of oxidation of refractory carbides. It is unknown if this

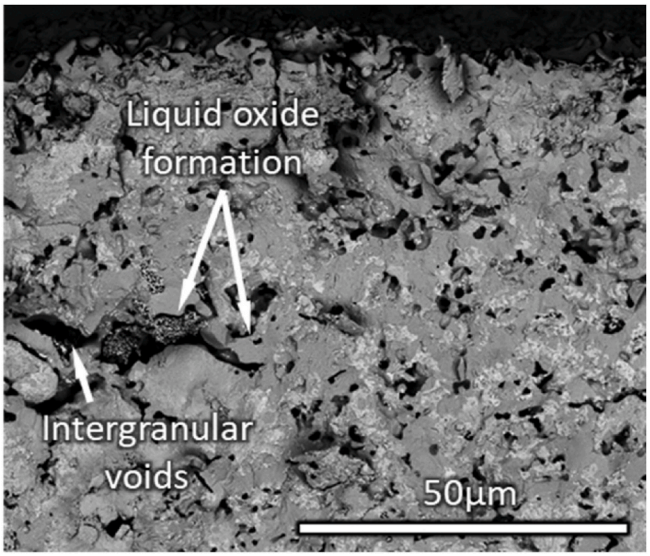

Fig. 16. Back-scattered electron image of the oxidized region fracture cross-section at the oxide/gas interface of (HfZrTiTaNb)C oxidized at 1700°C in 1% O2/Ar for 5 min.

played a role in the mode of attack of the different high entropy carbide compositions [9].

4.2. Borides

The high entropy diborides oxidized similarly (relative to each other), with a group IV rich external scale. The borides generally also exhibited lower material consumption than the carbides. All exhibited a partially oxidized region depleted in group IV elements and rich in group V and VI borides (depending on composition). The microstructure in the partially oxidized region formed on $(HfZrTiTaMo)B_2$ consisted of relatively fine boride grains and porosity. This partially oxidized region was also similar to that formed on $(HfZrTiMoW)B_2$, except for the retention of the secondary W-rich phase (Fig. 21). It is not clear to what extent the segregation of preferential segregation of W (in particular) to this phase affected the material consumption results, although this secondary phase also contained appreciable amounts of the group IV elements (see supplemental materials). All the high entropy diborides exhibit evidence of boria solidified from the melt on the surface, and potentially in the

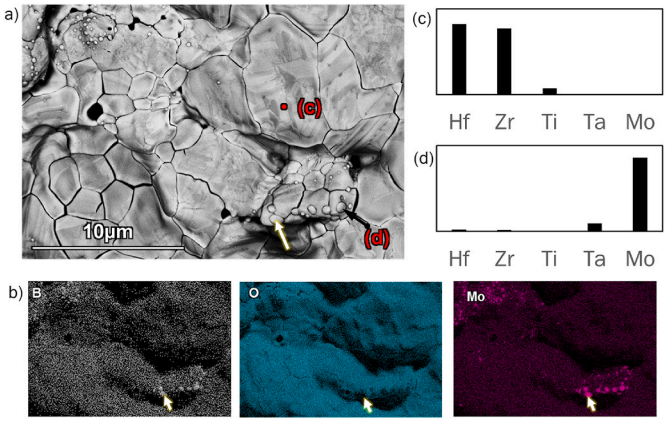

Fig. 18. (a) Backscattered electron image and (b) B, O and Mo EDS maps in plan view of $(HfZrTiTaMo)B_2$ oxidized at 1700°C in $1\%O_2$ for 5 min. (c) and (d) show point EDS analysis (arbitrary units) of the relative compositions of the two phases observed on the surface, respectively. Arrows show a Mo-rich feature.

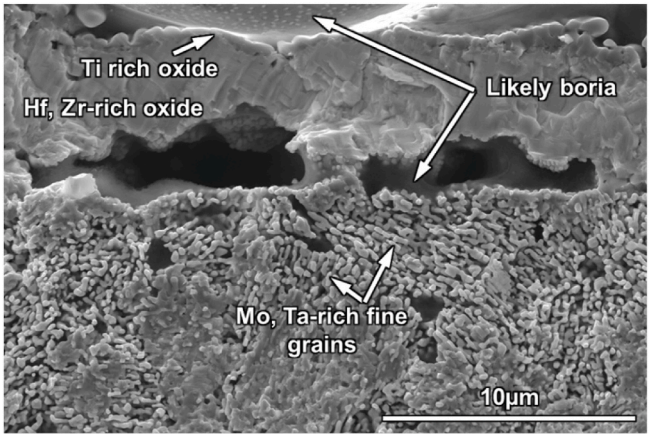

Fig. 19. (a) Secondary electron image of $(HfZrTiTaMo)B_2$ fracture cross-section, near the oxide/gas interface.

partially oxidized regions as well. The similarity of the material consumption (Fig. 10) and morphology of the oxidation affected regions among the high entropy borides suggests that the preferential oxidation of group IV elements along with the formation of boria could control the

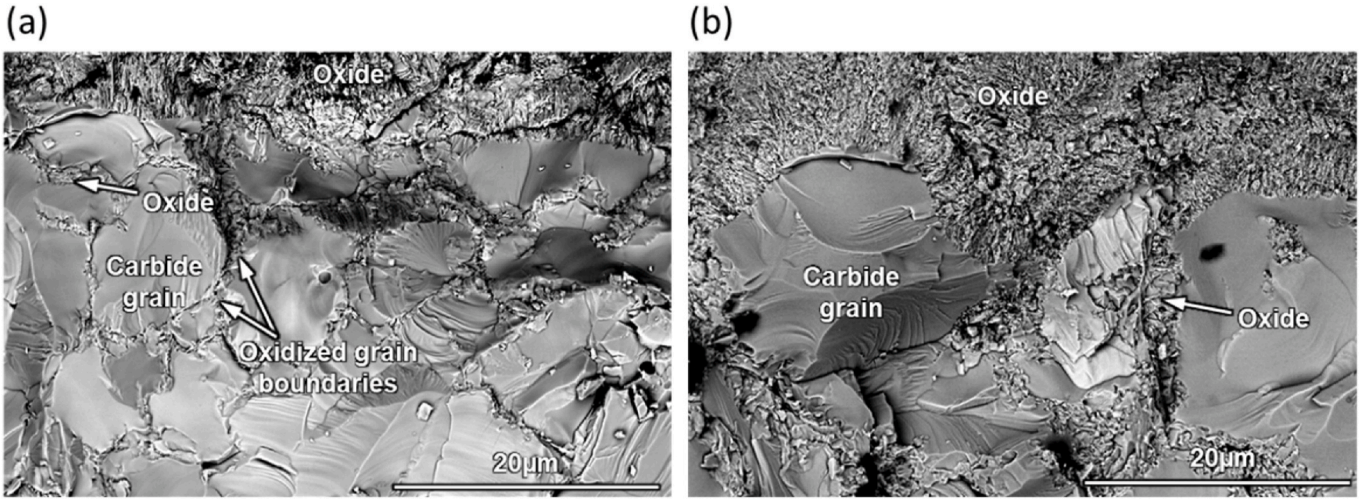

Fig. 17. Backscattered electron image fracture cross-section view of (a) (HfZrTiMoW)C and (b) (HfZrTiTaMo)C oxidized at 1700°C in $1\%O_2$/Ar for 5 min, at the oxide/substrate interface, showing intergranular oxidation.

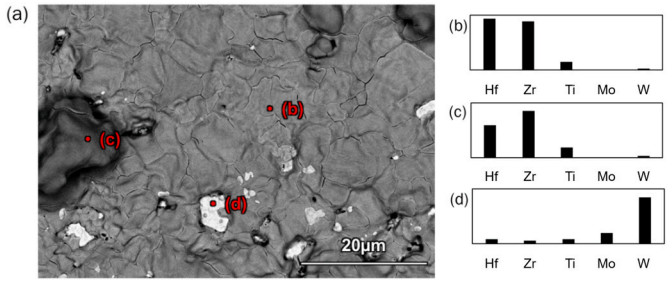

Fig. 20. (a) Backscattered electron image in plan view of (HfZrTiMoW)B_2 oxidized at 1700°C in 1%O_2 for 5 min (c), (d) and (e) show point EDS analysis of the phases observed on the surface.

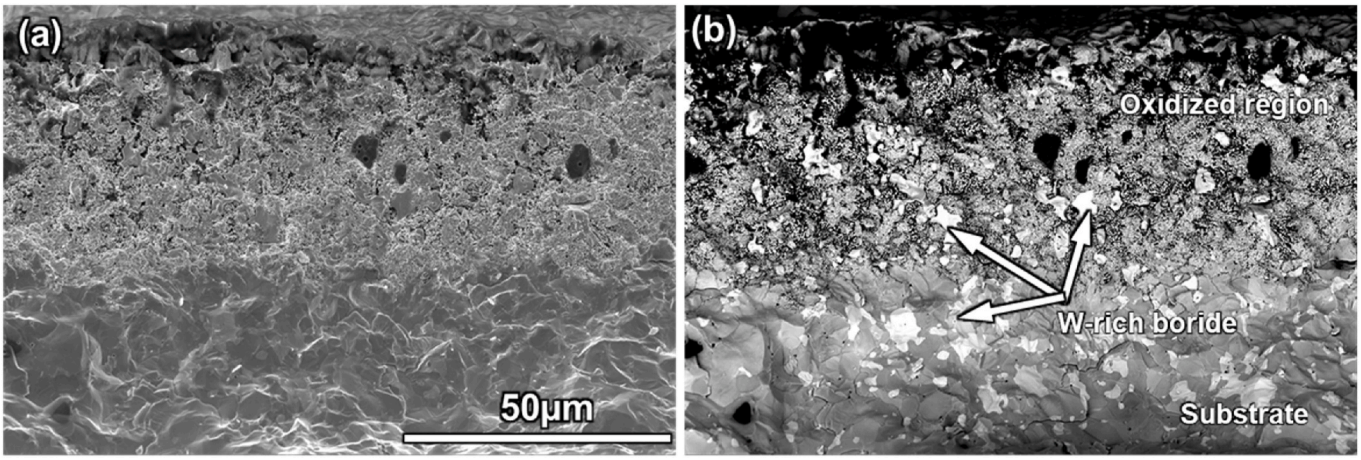

Fig. 21. (a) Secondary electron and (b) backscattered electron image of (HfZrTiMoW)B_2 fracture cross-section, after oxidation exposure at 1700°C in 1%O_2/Ar for 5 min.

oxidation behavior of these compounds.

4.3. Design of oxidation-resistant HE-UHTCs

A large advantage to the high entropy approach is the expansion of compositional space for UHTCs. However, the effect of configurational entropy in stabilizing the solid solution phase in a high entropy carbide or boride is negligible compared to the large, negative free energies of the oxidation reactions [8]. Nevertheless, high entropy compositions may still be pursued for potential improvements or tailoring of other properties, such as mechanical and thermal properties [42,52,53].

Periodic trends in oxidation behavior and oxide stabilities of the group IV, V and VI oxides were previously predicted [5,8] and verified to result in a tendency towards preferential oxidation occurring in these materials and destabilization of the underlying solid solution phase. This study has confirmed group IV elements, particularly Hf and Zr, which have the highest melting temperatures of the elements of interest, will form. These oxides are porous when formed on the carbide, and denser when formed on the diboride. A dense, adherent and solid scale is required for oxidation resistance. As the effects of CO(g) and volatile B_2O_3 (l,g) in forming a porous or otherwise disrupted scale cannot be discounted, the addition of elements that promote densification or sintering at ultra-high temperatures (UHTs) is required. The group V additions, Ta and Nb have been shown to promote liquid oxide formation which, if combined with effects such as gaseous (CO(g)) and volatile (MoO_3 (g)) oxide evolution, as seen in the composition (HfZrTiTaMo)C, resulted in large intergranular voids which were ultimately detrimental to the oxidation resistance of high entropy carbides. Ta additions were also proposed to promote the formation of complex oxides such as $Hf_6Ta_2O_{17}$, which may promote oxidation resistance. However, while there is evidence for the presence of such complex oxides, the results discussed here and for the oxidation of (HfZrTiTaNb)C [9], as well as in a more recent HfC-TaC oxidation study [11], show that excess Ta additions in materials that oxidize intergranularly (such as UHTC carbides) result in liquid oxide formation, which in turn promotes “premature” densification of the intergranular oxides (before an external scale can form). In the cases of Ta additions, oxygen transport towards the center of the grains in the oxidation-affected zone is slowed due to the densified intergranular oxide, while intergranular oxygen transport continues to occur into the unoxidized material.

The presence of group VI oxides in the thermally grown scale show that porosity due to volatile oxides is observed on the surface of the scale (Figs. 13 and 15), but the mode of attack was more uniform, despite evidence of preferential oxidation. The pores observed were just below the surface and smaller than that seen in the cross sections of group V containing compositions (e.g., Fig. 16). Any detrimental effects due to the non-group IV elements present in the oxide phase, in this case Mo and W, was minimized due to (a) their oxides having limited solubility in group IV oxides, being volatile and leaving the system, and (b) their preferential retention as a carbide phase. The material consumption data confirms that at the conditions tested, group VI additions to group IV base-material are preferable over group V additions. This is especially true for conditions that likely prevail during hypersonic flight. Thus, the group IV + VI elemental combination is a promising route for the design of HE-UHTCs.

Further, while preferential oxidation may be considered to result in destabilization of the solid solution substrate phase, it may also be a beneficial effect if the oxidation of non-group IV elements are limited, such as observed here for (HfZrTiMoW)C. The concept behind the compositional balance diagram and its extension using computational tools [8] can help tailor high entropy UHTC compositions away from the starting equimolar compositions or the five components discussed, that

may then aid in tailoring this preferential oxidation to limit non-group IV oxide formation.

All the diborides tested exhibited similar material consumption. Examination of the post-exposure morphology suggest that liquid boria plays a significant role in the ultra-high temperature oxidation behavior of refractory metal diborides. While borides have exhibited superior oxidation resistance compared to carbides in most of the results presented, this effect is not expected to hold at temperatures in excess of the boria boiling point (>1860°C [39,40]) at 1 atm. The extent to which this might be the case needs to be further probed in experiments at higher temperatures. It should be noted that the results presented in this paper were partially from samples wherein the presence of secondary phases such as B_4C may affect our understanding of the performance of pure metal diborides. Recent improvements in the synthesis of high entropy diborides to minimize secondary phases [42] should be leveraged to confirm these results.

5. Conclusions

High entropy UHTCs leverage a unique paradigm in materials design to develop materials with novel properties for use in extreme environments. The high entropy approach has been proposed as a way to design more oxidation-resistant UHTCs, which are needed for applications such as nuclear reactors and hypersonics. This work systematically investigated the oxidation resistance of multiple high entropy UHTC compositions, designed based on known trends in the oxidation behavior of their constituents. A unique experimental set-up using Joule heating was employed to expose the samples to a temperature of 1700°C in controlled pO_2 environments.

All the high entropy compositions exhibited preferential group IV oxidation. High entropy diborides exhibited more favorable oxidation resistance versus high entropy carbides for samples tested at 1700°C and 1%O_2. (HfZrTiMoW)C exhibited better oxidation resistance compared to the Ta containing high entropy carbides. The addition of Ta promotes the formation of liquid oxides, which results in intergranular voids presenting fast pathways for oxidant ingress. The oxidation behavior and resistance of the high entropy diborides are very similar to each other, likely due to the formation of Hf and Zr rich external scales and boria.

These results have implications for the design of oxidation-resistant high entropy UHTCs. The inclusion of group V elements to carbide HE-UHTCs, at least in equimolar concentrations, is not recommended. The inclusion of group VI elements is more promising, although further optimization is needed. More work is needed to understand how well the diborides will perform at temperatures above the boria boiling point.

Declaration of competing interest

The authors declare that they have no known competing financial interests or personal relationships that could have appeared to influence the work reported in this paper.

Acknowledgements

This work is supported by the U.S. Office of Naval Research MURI program (grant no. N00014-15- 1-2863) and the Virginia Space Grant Consortium Graduate Research Fellowship. J.L. and M.Q. also acknowledge partial support of National Science Foundation (NSF) Materials Research Science and Engineering Center program through the UC Irvine Center for Complex and Active Materials (CCAM) via NSF grant no. DMR-2011967 currently (for 2020–2026) after the completion of the MURI project. Bulk carbide samples were provided by the Vecchio research group at the University of California San Diego. Microscopy and X-ray diffraction was conducted at the Nanoscale Materials Characterization Facility at the University of Virginia.

Appendix A. Supplementary data

Supplementary data to this article can be found online at https://doi.org/10.1016/j.oceram.2024.100563.

References

[1] E. Wuchina, E. Opila, M. Opeka, W. Fahrenholtz, I. Talmy, UHTCs: ultra-high temperature ceramic materials for extreme environment applications, Electrochem. Soc. Interface 16 (2007) 30.
[2] E. Castle, M. Reece, S. Grasso, T. Csanadi, J. Dusza, High Entropy Transition Metal Carbides, 2017.
[3] T.J. Harrington, High Entropy Carbides: Modeling, Synthesis, and Properties, 2019. Ph.D. Dissertation, UC San Diego.
[4] J. Gild, Y. Zhang, T. Harrington, S. Jiang, T. Hu, M.C. Quinn, W.M. Mellor, N. Zhou, K. Vecchio, J. Luo, High-entropy metal diborides: a new class of high-entropy materials and a new type of ultrahigh temperature ceramics, Sci. Rep. 6 (2016).
[5] L. Backman, E.J. Opila, Thermodynamic assessment of the group IV, V and VI oxides for the design of oxidation resistant multi-principal component materials, J. Eur. Ceram. Soc. 39 (2019) 1796–1802.
[6] M.M. Opeka, I.G. Talmy, J.A. Zaykoski, Oxidation-based materials selection for 2000°C + hypersonic aerosurfaces: theoretical considerations and historical experience, J. Mater. Sci. 39 (2004) 5887–5904.
[7] V. Cirilli, A. Burdese, C. Brisi, Atti Accad. Sci. Torino, Cl Sci. Fis., Mat. Nat 95 (1961) 197–228.
[8] L. Backman, J. Gild, J. Luo, E.J. Opila, Part I: theoretical predictions of preferential oxidation in refractory high entropy materials, Acta Mater. 197 (2020) 20–27.
[9] L. Backman, J. Gild, J. Luo, E.J. Opila, Part II: experimental verification of computationally predicted preferential oxidation of refractory high entropy ultra-high temperature ceramics, Acta Mater. 197 (2020) 81–90.
[10] J. Zhang, S. Wang, W. Li, Y. Yu, J. Jiang, Understanding the oxidation behavior of Ta–Hf–C ternary ceramics at high temperature, Corrosion Sci. (2019) 108348.
[11] C. Zhang, High Temperature Oxidation Study of Tantalum Carbide-Hafnium Carbide Solid Solutions Synthesized by Spark Plasma Sintering, Florida International University, 2016. Ph.D. Dissertation.
[12] Y. Zeng, D. Wang, X. Xiong, X. Zhang, P.J. Withers, W. Sun, M. Smith, M. Bai, P. Xiao, Ablation-resistant carbide $Zr_{0.8}Ti_{0.2}C_{0.74}B_{0.26}$ for oxidizing environments up to 3,000°C, Nat. Commun. 8 (2017) 15836.
[13] E. Opila, Levine S and Lorincz J Oxidation of ZrB_2- and HfB_2-based ultra-high temperature ceramics: effect of Ta additions, J. Mater. Sci. 39 (2004) 5969–5977.
[14] C. Gasparrini, R.J. Chater, D. Horlait, L. Vandeperre, W.E. Lee, Zirconium carbide oxidation: kinetics and oxygen diffusion through the intermediate layer, J. Am. Ceram. Soc. 101 (2018) 2638–2652.
[15] S. Shimada, K. Mochidsuki, The oxidation of TiC in dry oxygen, wet oxygen, and water vapor, J. Mater. Sci. 39 (2004) 581–586.
[16] A. Münster, Über die Oxydation metallischer Hartstoffe, Zeitschrift für Elektrochemie, Berichte der Bunsengesellschaft für physikalische Chemie 63 (1959) 807–818.
[17] M. Desmaison-Brut, N. Alexandre, J. Desmaison, Comparison of the oxidation behaviour of two dense hot isostatically pressed tantalum carbide (TaC and Ta_2C) Materials, J. Eur. Ceram. Soc. 17 (1997) 1325–1334.
[18] A. Szokefalvi-Nagy, H. Jehn, High-temperature oxidation of NbC and TaC at low oxygen pressures, Z. Metallkd. 75 (1984) 389–394.
[19] L. Silvestroni, S. Guicciardi, C. Melandri, D. Sciti, TaB_2-based ceramics: microstructure, mechanical properties and oxidation resistance, J. Eur. Ceram. Soc. 32 (2012) 97–105.
[20] P. Kofstad, Low-pressure oxidation of tantalum at 1300°–1800°C, J. Less Comm. Met. 7 (1964) 241–266.
[21] H. Jehn, E. Olzi, High temperature solid-solubility limit and phase studies in the system tantalum-oxygen, J. Less Comm. Met. 27 (1972) 297–309.
[22] I.G. Talmy, J.A. Zaykoski, M.M. Opeka, S. Dallek, Oxidation of ZrB_2 ceramics modified with SiC and group IV–VI transition metal diborides Elec, Chem. Soc. Proc 12 (2001) 144–158.
[23] D. Sciti, L. Silvestroni, S. Guicciardi, D.D. Fabbriche, A. Bellosi, Processing, mechanical properties and oxidation behavior of TaC and HfC composites containing 15 vol% $TaSi_2$ or $MoSi_2$, J. Mater. Res. 24 (2009) 2056–2065.
[24] L. Silvestroni, A. Vinci, S. Failla, L. Zoli, V. Rubio, J. Binner, D. Sciti, Ablation behaviour of ultra-high temperature ceramic matrix composites: role of $MeSi_2$ addition, J. Eur. Ceram. Soc. 39 (2019) 2771–2781.
[25] E. Sani, L. Mercatelli, J.-L. Sans, L. Silvestroni, D. Sciti, Porous and dense hafnium and zirconium ultra-high temperature ceramics for solar receivers, Opt. Mater. 36 (2013) 163–168.
[26] A Yu Potanin, S. Vorotilo, S. Pogozhev Yu, S.I. Rupasov, P.A. Loginov, N. V. Shvyndina, T.A. Sviridova, E.A. Levashov, High-temperature oxidation and plasma torch testing of $MoSi_2$–HfB_2–MoB ceramics with single-level and two-level structure, Corrosion Sci. 158 (2019) 108074.
[27] S. Guo, T. Mizuguchi, M. Ikegami, Y. Kagawa, Oxidation behavior of ZrB_2–$MoSi_2$–SiC composites in air at 1500°C, Ceram. Int. 37 (2011) 585–591.
[28] D. Sciti, A. Balbo, A. Bellosi, Oxidation behaviour of a pressureless sintered HfB_2–$MoSi_2$ composite, J. Eur. Ceram. Soc. 29 (2009) 1809–1815.
[29] L. Charpentier, M. Balat-Pichelin, D. Sciti, L. Silvestroni, High temperature oxidation of Zr- and Hf-carbides: influence of matrix and sintering additive, J. Eur. Ceram. Soc. 33 (2013) 2867–2878.

[30] L. Silvestroni, K. Stricker, D. Sciti, H.-J. Kleebe, Understanding the oxidation behavior of a ZrB_2–$MoSi_2$ composite at ultra-high temperatures, Acta Mater. 151 (2018) 216–228.
[31] M. Kazemzadeh Dehdashti, W.G. Fahrenholtz, G.E. Hilmas, Effects of transition metals on the oxidation behavior of ZrB_2 ceramics, Corrosion Sci. 91 (2015) 224–231.
[32] D.-L. Yung, B. Maaten, M. Antonov, I. Hussainova, Oxidation of spark plasma sintered ZrC-Mo and ZrC-TiC composites, Int. J. Refract. Metals Hard Mater. 66 (2017) 244–251.
[33] M. Kazemzadeh Dehdashti, W.G. Fahrenholtz, G.E. Hilmas, Effects of temperature and the incorporation of W on the oxidation of ZrB_2 ceramics, Corrosion Sci. 80 (2014) 221–228.
[34] C.M. Carney, T.A. Parthasarathy, M.K. Cinibulk, Oxidation resistance of hafnium diboride ceramics with additions of Silicon carbide and tungsten boride or tungsten carbide, J. Am. Ceram. Soc. 94 (2011) 2600–2607.
[35] S.C. Zhang, G.E. Hilmas, W.G. Fahrenholtz, Improved oxidation resistance of zirconium diboride by tungsten carbide additions, J. Am. Ceram. Soc. 91 (2008) 3530–3535.
[36] L. Silvestroni, D. Sciti, F. Monteverde, K. Stricker, H.-J. Kleebe, Microstructure evolution of a W-doped ZrB_2 ceramic upon high-temperature oxidation, J. Am. Ceram. Soc. 100 (2017) 1760–1772.
[37] L.L.Y. Chang, M.G. Scroger, B. Phillips, Condensed phase relations in the systems ZrO_2-WO_2-WO_3 and HfO_2-WO_2-WO_3, J. Am. Ceram. Soc. 50 (1967) 211–215.
[38] G.R. Holcomb, The High Temperature Oxidation of Hafnium-Carbide, The Ohio State University, 1988. Ph.D. Dissertation.
[39] A.G. Metcalfe, Gas evolution during oxidation of refractory borides and carbides at 1500°C to 2700°C, ECS Trans. 3 (2007) 131–142.
[40] S.S. Cole, N.W. Taylor, THE SYSTEM Na_2O-B_2O_3, IV vapor pressures of boric oxide, sodium metaborate, and sodium diborate between 1150°C and 1400°C, J. Am. Ceram. Soc. 18 (1935) 82–85.
[41] T.A. Parthasarathy, R.A. Rapp, M. Opeka, R.J. Kerans, A model for the oxidation of ZrB_2, HfB_2 and TiB_2, Acta Mater. 55 (2007) 5999–6010.
[42] J. Gild, A. Wright, K. Quiambao-Tomko, M. Qin, J.A. Tomko, M. Shafkat bin Hoque, J.L. Braun, B. Bloomfield, D. Martinez, T. Harrington, K. Vecchio, P. E. Hopkins, J. Luo, Thermal conductivity and hardness of three single-phase high-entropy metal diborides fabricated by borocarbothermal reduction and spark plasma sintering, Ceram. Int. 46 (5) (2019) 6906–6913.
[43] E.A. Gulbransen, Thermochemistry and the oxidation of refractory metals at high temperature, Corrosion 26 (1970) 19–28.
[44] A. Jongejan, A.L. Wilkins, A re-examination of the system Nb_2O_5-TiO_2 at liquidus temperatures, J. Less Comm. Met. 19 (1969) 185–191.
[45] R.S. Roth, L.W. Coughanour, Phase equilibrium relations in the systems titania-niobia and zirconia-niobia, J. Res. Natl. Bur. Stand. 55 (1955) 209.
[46] J.L. Waring, R.S. Roth, Effect of oxide additions on polymorphism of tantalum pentoxide (system Ta_2O_5-TiO_2), J. Res. Natl. Bur. Stand. Sect. A: Phys. Chem. 72A (1968) 175.
[47] S.J. McCormack, K.-P. Tseng, R.J.K. Weber, D. Kapush, S.V. Ushakov, A. Navrotsky, W.M. Kriven, -situ determination of the HfO_2–Ta_2O_5-temperature phase diagram up to 3000°C, J. Am. Ceram. Soc. 102 (2019) 4848–4861.
[48] W.L. Worrell, A Thermodynamic Analysis of the Cr-Co, Mo-Co, and W-Co Systems *Report*, University of California, Lawrence Radiation Laboratory, 1964.
[49] A. Warren, A. Nylund, I. Olefjord, Oxidation of tungsten and tungsten carbide in dry and humid atmospheres, Int. J. Refract. Metals Hard Mater. 14 (1996) 345–353.
[50] A.E. Newkirk, The oxidation of tungsten carbide, J. Am. Chem. Soc. 77 (1955) 4521–4522.
[51] A.S. Kurlov, A.I. Gusev, Oxidation of tungsten carbide powders in air, Int. J. Refract. Metals Hard Mater. 41 (2013) 300–307.
[52] R.-Z. Zhang, J. Reece M, Review of high entropy ceramics: design, synthesis, structure and properties, J. Mater. Chem. A 7 (39) (2019) 22148–22162.
[53] P. Sarker, T. Harrington, C. Toher, C. Oses, M. Samiee, J.-P. Maria, D.W. Brenner, K.S. Vecchio, S. Curtarolo, High-entropy high-hardness metal carbides discovered by entropy descriptors, Nat. Commun. 9 (2018) 1–10.